Dalton Transactions

ROYAL SOCIETY OF CHEMISTRY

PAPER

View Article Online
View Journal | View Issue

Cite this: *Dalton Trans.*, 2024, **53**, 6779

Coordination of copper within a crystalline carbon nitride and its catalytic reduction of CO_2†

Magnus Pauly,[a] Ethan White,[a] Mawuli Deegbey,[a] Emmanuel Adu Fosu,[a] Landon Keller,[b] Scott McGuigan,[a] Golnaz Dianat,[b] Eric Gabilondo,[a] Jian Cheng Wong,[c,d] Corban G. E. Murphey,[c] Bo Shang,[e] Hailiang Wang,[e] James F. Cahoon,[c] Renato Sampaio,[c] Yosuke Kanai,[c,d] Gregory Parsons,[b] Elena Jakubikova[a] and Paul A. Maggard*[a]

Inherently disordered structures of carbon nitrides have hindered an atomic level tunability and understanding of their catalytic reactivity. Starting from a crystalline carbon nitride, poly(triazine imide) or PTI/LiCl, the coordination of copper cations to its intralayer *N*-triazine groups was investigated using molten salt reactions. The reaction of PTI/LiCl within CuCl or eutectic KCl/$CuCl_2$ molten salt mixtures at 280 to 450 °C could be used to yield three partially disordered and ordered structures, wherein the Cu cations are found to coordinate within the intralayer cavities. Local structural differences and the copper content, *i.e.*, whether full or partial occupancy of the intralayer cavity occurs, were found to be dependent on the reaction temperature and Cu-containing salt. Crystallites of Cu-coordinated PTI were also found to electrophoretically deposit from aqueous particle suspensions onto either graphite or FTO electrodes. As a result, electrocatalytic current densities for the reduction of CO_2 and H_2O reached as high as ~10 to 50 mA cm^{-2}, and remained stable for >2 days. Selectivity for the reduction of CO_2 to CO *vs.* H_2 increases for thinner crystals as well as for when two Cu cations coordinate within the intralayer cavities of PTI. Mechanistic calculations have also revealed the electrocatalytic activity for CO_2 reduction requires a smaller thermodynamic driving force with two neighboring Cu atoms per cavity as compared to a single Cu atom. These results thus establish a useful synthetic pathway to metal-coordination in a crystalline carbon nitride and show great potential for mediating stable CO_2 reduction at sizable current densities.

Received 5th February 2024,
Accepted 21st March 2024

DOI: 10.1039/d4dt00359d

rsc.li/dalton

I. Introduction

The release of carbon dioxide (CO_2) from the burning of fossil fuels is a global issue, with our daily life tied to processes which release billions of metric tons of CO_2 per year. To address this, intense research has gone into the capture and conversion of CO_2 into chemical fuels. Research into carbon nitrides (CN_x) has surged in importance because of their promising catalytic activities for the reduction of carbon dioxide (CO_2R), such as when surface-impregnated or internally coordinated by metal cations (*i.e.*, m-CN_x). This growing new class of m-CN_x materials has shown a promising capability to assist in the electrocatalytic conversion of CO_2 to carbon monoxide, formate, and/or methanol.[1–9] However, currently known materials lack sufficient crystallinity for in depth structural characterization of the local coordination environments or determination of the relevant mechanistic pathways with deeper atomic-level detail.[7] Currently, nearly all relevant catalytic mechanisms have been probed computationally assuming idealized structural models.

Most studied carbon nitrides are layered but amorphous materials containing heptazine monomers with alternating sp^2 carbon and nitrogen atoms. The carbon to nitrogen ratio is typically C_3N_4, or otherwise known as graphic carbon nitride (g-C_3N_4), and which is postulated to consist of a mixture containing polymerized heptazine units, or poly(heptazine imide).[8,10–12] By contrast, a more crystalline carbon nitride is

[a]*North Carolina State University, Department of Chemistry, Raleigh, NC 27695, USA. E-mail: paul_maggard@ncsu.edu*
[b]*North Carolina State University, Department of Chemical Engineering, Raleigh, NC 27695, USA*
[c]*University of North Carolina-Chapel Hill, Department of Chemistry, Chapel Hill, NC 27599, USA*
[d]*University of North Carolina-Chapel Hill, Departments of Physics and Astronomy, Chapel Hill, NC 27599, USA*
[e]*Yale University, Department of Chemistry, New Haven, CT 06520, USA*

†Electronic supplementary information (ESI) available: Experimental and computational procedures, Rietveld refinements, elemental analysis, FT-IR, UV-Vis DRS, CO_2R product distributions, frontier molecular orbitals of intermediates, and reaction coordinate diagram. See DOI: https://doi.org/10.1039/d4dt00359d

known, poly(triazine imide) or PTI/LiCl ($C_6N_9H_2Li_2Cl$), consisting of triazine rings linked by imide bridges. Notably, it contains intralayer cavities with two Li and two H atoms each.[8,9] A recent study of the different possible Li/H configurations demonstrated a preferred cation ordering within its intralayer cavities.[10] The crystalline PTI/LiCl was also shown to possess the capability to coordinate a small amount of Cu cations with the maintenance of its structure.[10,13] However, relevant catalytic activity has not yet been fully investigated, such as for the reduction of carbon dioxide (CO_2R), as is known to occur for many Cu-containing materials. Driven either by light and/or by an applied bias, catalytic CO_2R has been intensely investigated for metallic Cu, Cu-containing molecular complexes, Cu on N-doped graphene, and for Cu(I) surface-attached to PHI/NaCl and carbon-based nanomaterials.[1–6,14,15] For example, recent light-driven catalytic studies on Cu-impregnated g-C_3N_4 have shown a high selectivity for CO production from CO_2R and absorption of CO_2 at the catalytic Cu sites.[16–18] In the case of electrocatalytic CO_2R, such as by Cu metal, a less-selective range of reduction products are generated, including CO, CH_4 and CH_3OH, and which require a relatively large negative applied bias.[19,20] While greater selectivity is shown by molecular complexes containing Cu at less negative reduction potentials, these suffer from smaller attainable current densities.[21] Other strategies have included the attachment of Cu complexes to electrode surfaces,[15,22,23] but nearly are known to decompose to metallic Cu nanoclusters under a negative applied bias. This occurs because of the tendency for reduced Cu sites, *i.e.*, Cu(0), to irreversibly de-ligate. Alternate strategies are thus needed to provide a more rigid and stable ligand structure for Cu-based catalyst sites.

Described herein is an investigation into the coordination of Cu cations within the structure of crystalline carbon nitride, poly(triazine imide) lithium chloride (PTI/LiCl), using a novel molten-salt-based approach and the resulting compositions and structures that retain its crystalline framework. The Cu-containing products, *i.e.*, PTI/Cu_xCl (x = 1 or 2), were further investigated for their electrocatalytic activity for CO_2 reduction (CO_2R) *via* a newly developed low-bias electrophoretic deposition of the crystallites onto conducting substrates. Thus, this approach leverages a molecular-level type approach combined with density functional theory calculations to yield deeper insights into mechanistic CO_2R pathways not previously achieved. It also demonstrates a creative new pathway to prepare carbon-nitride-based electrodes with long-term stability and sizable current densities for electrocatalytic reduction reactions.

II. Experimental

A. Chemical reagents

Melamine (Sigma-Aldrich) 99%, lithium chloride (Fischer Science Education) reagent grade, potassium chloride (Fluka Chemical) 99.5%, copper(I) chloride (Thermo-Scientific) 99%, copper(II) chloride (Fischer Scientific) 99%, potassium bicarbonate (Sigma-Aldrich) 99.7%, carbon dioxide (Arc3 Gases) 99.99%, argon (Arc3 Gases) 99.999%, isotopically carbon labeled potassium bicarbonate ($KH^{13}CO_3$) (Sigma-Aldrich) 98%, and isotopically carbon labeled carbon dioxide $^{13}CO_2$ (Sigma-Aldrich) 99%.

B. Preparation of PTI/Cu compounds

i. Synthesis of PTI/LiCl. The synthesis of PTI/LiCl was performed according to a previously reported procedure.[10] In brief, potassium chloride and melamine were combined in a 9 to 1 molar ratio in a mortar and pestle and ground together until homogenous. To this mixture was added a 12-fold molar excess of lithium chloride to give a net mass of ~300 mg. The powders were transferred into a fused-silica reaction vessel, then placed under applied vacuum and flame sealed. The powders may also be ground in air and placed into a 140 °C oven for 12 h to dry. The reaction vessel was approximately 10 inches long with a radius of 0.5 inches (Note: a relatively large volume-to-mass should be used as the reaction of melamine liberates ammonia and pressurizes the reaction vessel). The vessel was then placed vertically into a muffle furnace and heated at a rate of 10 °C min^{-1} until 470 °C was reached. This temperature was held for 36 h, after which the furnace was cooled at a rate of 2 °C h^{-1} until the temperature reached 350 °C. Next, the furnace was then shut off and allowed to radiatively cool to room temperature. The resulting sample typically appeared white to light beige. The reaction vessel was carefully cut open within a hood and behind shielding using a glass cutter. The product was collected and washed with de-ionized water to dissolve the excess salt and isolate the PTI/LiCl powder. It was further washed and centrifuged in de-ionized water until a clean PTI/LiCl powder was obtained, as judged by powder XRD and FTIR-ATR measurements.

ii. Synthesis of 1-PTI/LiCuCl. In an argon glovebox and into a mortar and pestle was placed anhydrous CuCl (melting point of ~426 °C) together with PTI/LiCl with a molar ratio of 2 : 1.[24] The powder was ground together until the mixture appeared to be homogenous. The resultant powder was then immediately loaded into a fused-silica reaction vessel and placed under applied vacuum and flame sealed. The reaction vessel was approximately 6 inches long with a radius of 0.5 inches. The vessel was then placed vertically into a muffle furnace and heated at a rate of ~10 °C min^{-1} until 450 °C. This temperature was held for 24 h after which the furnace was cooled at a rate of 2 °C min^{-1} until the temperature reached 300 °C. At this point the furnace was then shut off and allowed to radiatively cool to room temperature. The resulting product was isolated from the salt flux by washing multiples times in de-ionized water, once in ammonium hydroxide, and one final wash in de-ionized water. The wet **1**-PTI/LiCuCl was then dried by vacuum.

iii. 2-PTI/Cu_2Cl. In an argon glovebox and into a mortar and pestle was placed anhydrous CuCl together with KCl in a 2 : 1 molar ratio (eutectic melting point ~150 °C).[24] The salts were ground until homogeneous and then PTI/LiCl was added. The molar ratio of CuCl to PTI/LiCl was 2 to 1 or greater, to

ensure complete cation exchange of Li for Cu. The resultant powder was then immediately loaded into a fused-silica reaction vessel under applied vacuum and sealed. The reaction vessel was approximately 6 inches long and had a radius of 0.5 inches. The vessel was then placed vertically into a muffle furnace and heated at a rate of ~10 °C min^{-1} until reaching 280 °C. This temperature was held for 24 h after which the furnace was cooled at a rate of 2 °C min^{-1} until reaching 150 °C. At this point the furnace was then shut off and allowed to radiatively cool to room temperature. The resulting product was isolated from the salt flux by washing multiples times in de-ionized water, once in ammonium hydroxide, and one final wash in de-ionized water. The wet **2**-PTI/Cu_2Cl was then dried by vacuum.

iv. 3-PTI/HCuCl. In an argon glovebox and into a mortar and pestle was placed anhydrous $CuCl_2$ together with KCl in a 2 : 1 molar ratio (eutectic melting point ~360 °C).[24] The salts were ground until homogeneous and then PTI/LiCl was added. The molar ratio of $CuCl_2$ to PTI/LiCl was 2 to 1 or greater, to ensure the complete cation exchange of Li for Cu. The resultant powder was then immediately placed into a fused-silica reaction vessel and placed under applied vacuum and flame sealed. The reaction vessel was approximately 8 inches long and had a radius of 0.5 inches. The sample was then placed vertically into a muffle furnace and heated at rate of ~10 °C min^{-1} until 400 °C. This temperature was held for 24 h after which the furnace was cooled at a rate of 2 °C min^{-1} until the temperature reached 350 °C. At this point the furnace was then shut off and allowed to radiatively cool to room temperature. The resulting product was isolated from the salt flux by washing multiples times in de-ionized water, once in ammonium hydroxide, and one final wash in de-ionized water. The wet **3**-PTI/HCuCl was then dried by vacuum.

C. Characterization techniques

Powder X-ray diffraction (PXRD) data on the PTI/Cu materials were taken using Mo Kα radiation (λ = 0.7107 Å) from a sealed tube X-ray source (40 kV, 36 mA). The structures were refined within the software package GSAS-II. Additional details are described in the ESI.† Fourier transform infrared spectroscopy with attenuated total reflection (FTIR-ATR, Cary 630 FTIR Spectrometer) was used to characterize local organic functional groups. Raman spectroscopy was acquired by measurements consisting of 25 scans from 600 to 4000 cm^{-1}. Characterization by scanning electron microscopy (SEM) utilized a FEI Verios 460L field-emission instrument operated at 13 pA current and 0.5–2 kV electron landing energy with sample bias of 0.5 kV. X-ray photoelectron spectroscopy (XPS; Kratos Analytical Axis Ultra) with an Al Kα (1486.6 eV) gun was operated at 10 mA and 15 kV. All spectra were calibrated by shifting the adventitious C 1s peak to 248.8 eV. The survey spectra and high-resolution scans for C 1s, N 1s, Cu 2p, Cu LMM were acquired. Nuclear magnetic spectroscopy (NMR; Bruker Avance NEO) was taken at 600 MHz. Dynamic light scattering measurements were used to assess particle size in solution with a Malvern Panalytical Nano-Zetasizer.

D. Electrocatalytic CO_2 reduction

A quartz H-cell was utilized that consisted of two ~15 ml cells connected by a bipolar membrane (Fumasep FBM). The head space was sealed by a compression top with four ports, a gas inlet (fritted), gas outlet, sampling septa, and a glassy carbon electrode. The oxidation cell is fitted with a platinum wire counter electrode and Ag/AgCl(sat) reference electrode. The buffer solution in the electrode compartments consisted of ~10 mL of 0.5 M potassium bicarbonate ($KHCO_3$) at pH ~6.8. Samples were purged with CO_2 then the applied bias was swept from 0 to −1.7 V *vs.* Ag/AgCl(sat). All electrochemical experiments were performed using a Pine instruments WaveDriver 200 EIS Bipotentiostat/Galvanostat from 0 to −1.7 V *vs.* Ag/AgCl(sat).

To prepare the polycrystalline electrodes, a buffered (0.5 M $KHCO_3$ in DI water) slurry of the carbon nitride material (~40 mmol) was stirred at 1000 rpm. An FTO slide was placed horizontally, face down, just below the meniscus of the slurry solution. Bulk electrolysis at −1.4 V *vs.* Ag/AgCl(sat) was then run for 90 min, after which the electrode was allowed to air dry prior to its use. The identification and quantification of gaseous reaction products were performed with an Agilent 8890 gas chromatograph. A custom-built inline valve system and column configuration of the GC is illustrated in the ESI.† A carbon plot (column 1) and a mol sieves (column 2) column were installed in series through switching valves. The carbon plot decelerates the elution of CO_2 relative to other gases such as O_2, N_2, H_2, and CO. The mol sieves column is used for separation of gaseous products with specific retention times. A thermal conductivity detector was used to primarily monitor O_2, N_2, and H_2. A methanizer (nickel hydrogenation catalyst) was paired with a flame ionization detector for enhanced sensitivity to detect CO, which is done in series with the TCD measurements. Argon was used as the carrier gas. Details of the GC valve configuration are given in the ESI.†

E. Computational methodologies

As the starting point of GW calculations, density functional theory (DFT) calculations were performed using Quantum ESPRESSO code.[25–27] The Kohn–Sham (KS) wave functions were represented in a plane-wave basis using the norm-conserving ONCV pseudopotentials with a kinetic energy cutoff of 50 Ryd. PBE0 hybrid exchange–correlation approximation was used in the calculations.[28–31] Using the KS orbitals and energies, quasiparticle (QP) energies were obtained by performing GW method calculation within the G_0W_0 approximation using the BerkeleyGW code.[32] Hybertsen–Louie generalized plasmon pole model was used to model the dielectric function and random phase approximation was used for the screened Coulomb interaction.[25] The GW calculations were converged to within 1 k_BT with respect to parameters. An 80-atom supercell with periodic boundary conditions (PBC) was used for the calculation of the bulk PTI system. The dimension of the supercell used was 14.67 Å × 8.47 Å × 6.72 Å, and it consisted of two layers of PTI in the A1a structure in space group *Ama2*.[10] Each layer contained two pores with the cation located

in-plane within the PTI layer while the halides were intercalated in between the pores of the two PTI layers. A 2 × 4 × 4 Monkhorst–Pack *k*-point grid was used for sampling the Brillouin zone.[33] The two-dimensional monolayer of PTI was modeled using a 36-atom supercell, and its dimension was 14.67 Å × 8.47 Å × 20.00 Å. One cation atom was removed from each pore of the PTI to ensure that the system remained charge neutral. While PTI/Cu can have up to two Cu cations per pore, the use of PBC in the calculation makes it difficult to model this kind of charge non-neutral situation. The calculations were performed using a 2 × 4 × 1 *k*-point grid sampling the Brillouin zone.

For calculation of the mechanistic pathway of CO_2 reduction, DFT methods utilizing the B3LYP functional were employed for optimization of all complexes in this study.[34] Note that a molecular model of a single pore was employed in these calculations that allowed convenient accounting for solvent effects as well as the charge changes at the catalytic center due to the reduction events and proton transfers. Additionally, the basic electronic structure of the molecular model was in close agreement with the electronic structure for the monolayer, with the frontier orbitals (HOMO and LUMO) being localized on the two Cu atoms. The 6-311G* basis set was used for all atoms (H, C, N, O), except for Cu, where the Stuttgart-Dresden (SDD) basis sets and its accompanying pseudopotential was employed.[35–37] Solvent effects (water) were included in all the calculations *via* the polarizable continuum model (PCM).[38] Vibrational frequency analysis was performed to ensure that the optimized structures correspond to minima on their respective potential energy surfaces. The frequency calculations were also used to obtain zero-point energies and entropic corrections to the free energy (assuming a temperature of 298.15 K and 1.0 atm, respectively) using standard statistical mechanical conventions. The calculated reduction potentials (E°) were determined relative to the ferrocene couple through eqn (1):

$$E^\circ(\text{in V}) = -\frac{\Delta G_{\text{sol}}}{nF} - 5.25 \quad (1)$$

where ΔG_{sol} is the change in solvated free energy upon reduction, n is the number of electrons (in this case, 1), and F is the Faraday constant. The calculated half-cell potential for the ferrocene couple (5.25 V) was obtained by using the same level of theory as that of the complexes since this reduces the errors in the calculated redox potential.[39] In order to report the redox potential *vs.* SHE, a 0.45 V correction factor was added. All calculations were carried out using the Gaussian 16, Revision A.03 software package.[40]

III. Results and discussion

A. Synthesis and structural characterization

Reactions of low-melting molten salts containing the Cu(I)/Cu(II) cations were performed under vacuum and resulted in the partial to complete exchange with the Li cations in PTI/LiCl. Specifically, crystalline PTI/LiCl was found to react within eutectic mixtures of either CuCl/KCl (60 : 40; **1** reacted at 450 °C and **2** reacted at 280 °C) or $CuCl_2$/KCl (55 : 45; **3** reacted at 350 °C), yielding the chemical compositions of **1**-PTI/LiCuCl, **2**-PTI/Cu_2Cl, or **3**-PTI/HCuCl, respectively. Powder XRD data of each showed significant differences, with structure refinements yielding slightly different Cu-coordination configurations and compositions within their intralayer cavities. Plots of Rietveld refinements of their powder XRD data are provided in the ESI.† Generally, the structures of **1–3** showed the maintenance of the underlying carbon nitride framework upon coordination by the Cu cations, where each structure contains either one or two of the three types of layers visualized in Fig. 1. All three types of layers exhibit a similar near-hexagonal pattern of intralayer cavities, each built from six triazine units that link through imide bridges. In PTI/LiCl, the intralayer cavities contain only H and Li cations. After exchange with Cu cations, each intralayer cavity contains up to two Cu cations coordinated to the *N*-triazine groups.

A predominant difference in each of the Cu-coordinated carbon nitride materials was in the number (0, 1 or 2) of Cu atoms contained within each intralayer cavity. Each intralayer cavity has three chelating imide-bridged *N*-triazine sites for coordination to multiple Cu cations. Results of elemental analysis, Table S2,† reveal that **1** and **3** contain one Cu per intralayer cavity (on average), while **2** consists of two Cu per intralayer cavity. The refined crystal structure of **1**-PTI/LiCuCl showed a best fit that was consistent with the partially-disordered structure previously reported in space group $Cmc2_1$,[10,41] in which two metal cations are disordered over the three crystallographic sites, illustrated in Fig. 1A. Thus, the structure contained one Cu cation, on average, per intralayer cavity, consistent with EDS data. By contrast, EDS analysis of the products obtained from the lower-melting CuCl/KCl salt flux at 280 °C revealed double the amount of Cu, or two Cu atoms per intralayer cavity. Structural refinements for this compound, **2**-PTI/Cu_2Cl, were attempted for each of the possible ordered configurations previously reported for Li,[10] but with replacement by Cu in each case. The results are listed in Table S1,† with space group, wR% of fitting, and references for the published models. Of these, the structural model showing the generally best fit to the experimental pattern was obtained in space group $P2_1/m$, which accounted for all diffraction peaks. The intralayer cavities of **2**-PTI/Cu_2Cl thus contained two ordered Cu atoms, shown in Fig. 1B. The two Cu are separated at ~3.72 Å, and both in a tetrahedral coordination environment consisting of Cu–Cl (×2; not shown in Fig. 1 for clarity) and Cu–N (×2). Thus, the reaction temperature and type of flux was observed to control the amount of Cu coordinated within the intralayer cavities.

By contrast, the Cu-containing PTI material from the reaction in $CuCl_2$/KCl at 350 °C, *i.e.*, **3**-PTI/HCuCl, exhibited marked changes in its diffraction pattern. Rietveld refinements of **3**-PTI/HCuCl could not be matched with any of the reported, 20 possible ordered or partially-disordered polymorphs.[9,10] Attempted structural refinements instead revealed a mixture of

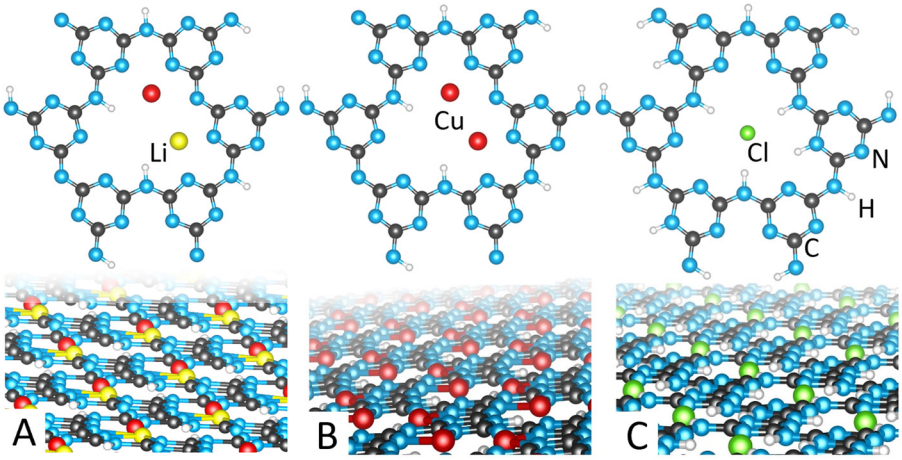

Fig. 1 Extended structural views of single layers (lower) and isolated intralayer cavities (upper) of the Cu-containing layers for (A) **1**-PTI/LiCuCl (1 Cu, 1 Li), (B) **2**-PTI/Cu_2Cl (2 Cu, 0 Li) and the additional delithiated layer (C) only present in the structure of **3**-PTI/HCuCl.

two types of layers, Fig. 1(B and C), that pack together. One consisted of a de-lithiated layer wherein the chloride anion is located within the cavity surrounded by four N–H protons, Fig. 1C, as reported previously for the structure of PTI·HCl.[11,12] The other layer contains two Cu cations per cavity at ~3.89 Å apart, Fig. 1B, in a tetrahedral coordination environment with Cu–Cl and Cu–N (×2 for each), similar to that described above in **2**. With a 50 : 50 ratio of the two layers, this structure also yields an average of ~1 Cu atom per cavity, though, with half of the layers containing two Cu cations. The refined chemical compositions of each of the PTI/Cu materials, **1**, **2** and **3**, were consistent with results from SEM-EDX and elemental analyses, given in the ESI.† The FT-IR, Fig. S1 in the ESI,† exhibited an increased N–H stretched region corresponding with the greater H content expected for the composition of **3**-PTI/HCuCl.

B. Electrophoretic deposition of catalyst films

The attainment of relatively well characterized Cu-coordination sites within the structure of PTI motivated subsequent investigations into the impact of Cu coordination and content (*i.e.* 1 or 2 Cu cations per cavity) on the selectivity of CO_2 reduction (CO_2R) *versus* H_2O reduction, as well as selectivity of product formation from CO_2R. Measurements of CO_2R by these compounds were conducted by leveraging a new low-bias, electrophoretic deposition of their crystallite particles from an aqueous 0.5 M $KHCO_3$ solution. While the electrophoretic deposition technique is known to be advantageous for the deposition of soft materials onto complex geometries, it has previously been reported to typically require 100's of volts to achieve particle deposition.[42] Owing to the charged layers of Cu-coordinated PTI, its crystallites could be deposited at just −1.4 V *versus* Ag/AgCl in an H-cell cathodic compartment, Fig. 2A (inset) after 90 min. SEM images in Fig. 3(A and B) of **3**-PTI/HCuCl films after 90 min show well-formed crystallites with dimension ~250 nm. This imaging confirms that smaller crystal particles deposit during the early stages of growth, with larger crystallites depositing at relatively longer times during the process.

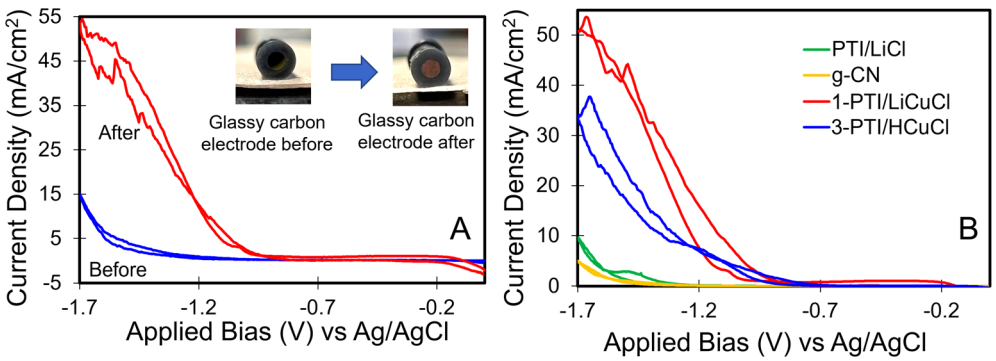

Fig. 2 (A) Cyclic voltammograms of a glassy carbon electrode placed in a 0.5 M solution of $KHCO_3$ and suspended particles of **1**-PTI/LiCuCl were measured before and after a 90 min electrophoretic deposition, and (B) a stack plot of cyclic voltammograms after 90 min electrophoretic deposition of paticles of **1**-PTI/LiCuCl, **3**-PTI/HCuCl and the controls of PTI/LiCl and graphitic carbon nitride (g-C_3N_4).

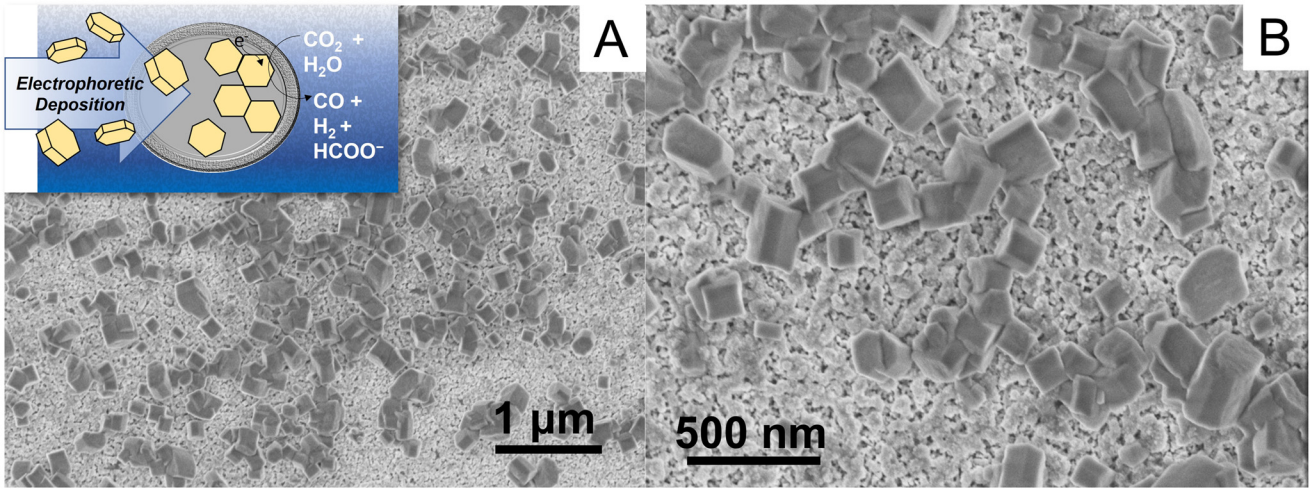

Fig. 3 (A and B) SEM image of **3**-PTI/HCuCl particles deposited onto an FTO electrode after 90 min electrophoretic deposition, showing the characteristic hexagonal, rod-shaped crystals. The inset is a generalized schematic of the deposition process.

C. Catalytic CO_2 reduction measurements

The crystallites were deposited onto either FTO or glassy carbon over the course of 90 min. After deposition, cathodic current densities of ~1 to 5 mA cm^{-2} were measured at −1.4 V *vs.* Ag/AgCl, consistent with the electrocatalytic reduction of protons and CO_2. Afterwards, the electrodes showed a significantly enhanced current density of ~30 to 50 mA cm^{-2} at −1.7 V *vs.* Ag/AgCl, Fig. 2A. By comparison, neither PTI/LiCl nor g-CN showed a similar current density under identical conditions, Fig. 2B, confirming the deposition and CO_2R catalytic activity arises from the Cu-containing PTI. The cyclic voltammograms (CV) measured using electrodes without deposited catalyst showed much smaller current densities. Chronoamperometry measurements using **3**-PTI/HCuCl were conducted at three applied biases, and the results are shown in Fig. 4A. At too low of an applied bias very small amounts of H_2 and CO were observed, while at a high applied bias the films delaminated quickly. An applied bias of −1.4 V *vs.* Ag/AgCl was found to be optimal because the current density increased linearly with time, demonstrating the films and catalytic activity remained stable. Control experiments in a NaCl buffered solution in the absence CO_2 and $KHCO_3$ showed only H_2 was produced.

Observed CO_2R products at −1.4 V *vs.* Ag/AgCl gave faradaic efficiencies (FE) that differed greatly depending on the Cu content, Fig. 5A. Between **1**-PTI/LiCuCl and **2**-PTI/Cu_2Cl the primary difference was the Cu content, *i.e.*, one Cu *versus* two Cu cations per PTI pore, respectively. Plotted in Fig. 5, product selectivity for one *versus* two Cu per pore included CO (15% *versus* 10%, respectively), formate (14% *versus* 45%), and H_2 (71% *versus* 45%). Thus, two Cu atoms per pore significantly increased formate selectivity and a higher selectivity for CO_2 reduction overall. Labeling studies using ^{13}C were conducted in duplicate with 0.5 M $KH^{13}CO_3$ and $^{13}CO_2$ as carbon sources and confirmed the origin of formate as arising from CO_2R, given in the ESI (Fig. S13 and S14†). Overall cathodic currents remained largely the same. In the case of **3**-PTI/HCuCl, the observed product selectivity of formate, CO, and H_2 were approximately 18, 13, and 69%,

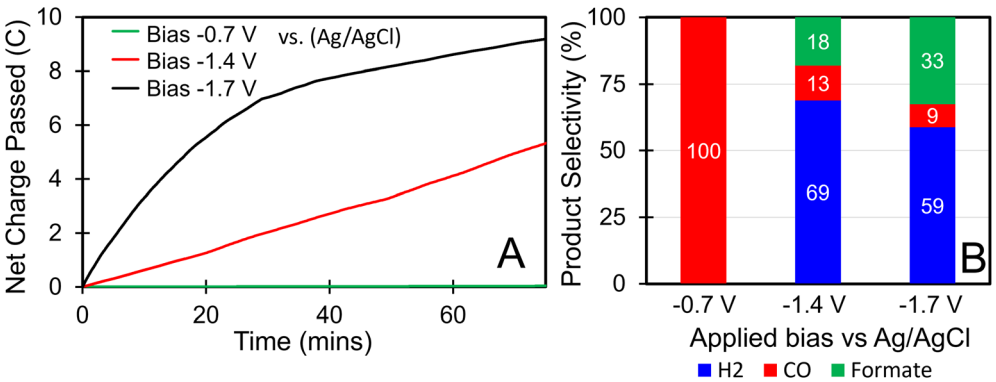

Fig. 4 (A) Chronoamperometry experiments on particles of **3**-PTI/HCuCl deposited onto an FTO electrode at three applied biases for 90 min, and (B) the corresponding product selectivity at each applied bias of −0.7 V, −1.4 V and −1.7 V *vs.* Ag/AgCl.

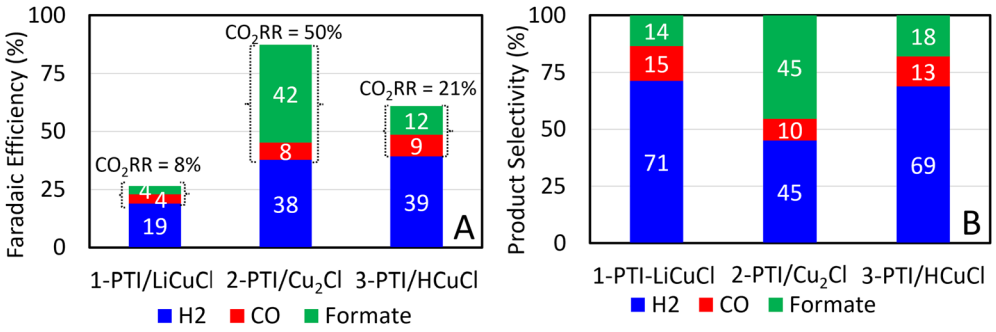

Fig. 5 (A) Faradaic efficiencies for each of the three different PTI/Cu materials deposited as particles onto an FTO electrode at −1.4 V *vs.* Ag/AgCl for 90 min in a buffered solution of 0.5 M $KHCO_3$ purged with CO_2. Each measurement was taken multiple times and averaged, with plots of (B) the corresponding product selectivities for H_2, CO and formate.

respectively. Only in the case where the PTI/Cu catalyst contained two Cu atoms per pore was a greater FE of CO_2R products observed.

Another factor impacting CO_2R was crystallite size. In electrophoretic deposition it is established that the smallest crystallites will deposit the fastest.[42,43] Therefore, films with different crystal sizes can be readily obtained by sequentially depositing crystal films from a single starting slurry. When **3**-PTI/HCuCl was sequentially deposited from the same starting slurry onto three FTO electrodes, the FE varied as a function of crystal size. A larger amount of CO_2R was found to occur with the smallest crystallites deposited from a fresh solution of the aqueous suspension, Fig. 6A. In the first run (run 1), the smallest particles have been extracted from solution, thereby leaving larger PTI/Cu particles to deposit from solution in the subsequent runs (runs 2 and 3). This sequence of larger PTI/Cu particles was confirmed using dynamic light scattering Fig. 6B. As these sequential depositions resulted in increasingly larger crystallites on the substrate, the FE for CO_2R decreased from 35 and 42% in runs 1 and 2, to a much lower 14% in run 3. A range of crystallite sizes depositing from solution also likely leads to particle distribution inhomogeneities and to the FE varying within ±10% between CO_2R experiments. Computational approaches were used to understand these trends in CO_2R, described below.

While electron microscopy confirmed the crystallite morphologies and elemental compositions remained stable and unchanged during the CO_2R experiments, XPS measurements were used to assess the possible changes in the Cu oxidation states and coordination environments closer to the surfaces. XPS data confirm that the relative atomic % of N, Cu, Cl and Li remain consistent both before and after CO_2R experiments, as given in the ESI.† After CO_2R, the *ex situ* XPS data in Fig. 7(A and B) show the Cu(I) feature remains dominant to the Cu(II) feature, and the Auger Cu $L_3M_{45}M_{45}$ parameter (Fig. S9 in the ESI†) is consistent with CuCl and $CuCl_2$ bonding environments before and after CO_2R, in agreement with the coordination environment of the Cu cation in **3**-PTI/HCuCl.[44] The post-reaction FT-IR data also maintain absorbance peaks consistent with the PTI/LiCl structure and functional groups, shown in Fig. S12.† These data confirm that both the crystallites and their Cu-coordination sites within the intralayer cavities at the surfaces of the carbon nitride are either maintained, or reversibly recovered, before and after the CO_2R experiments.

D. Electronic structure and mechanistic calculations

First-principles electronic structure theory was employed to analyze both the bulk and two-dimensional (2D) monolayer form of PTI/Cu for insights into how the substitution of Li for

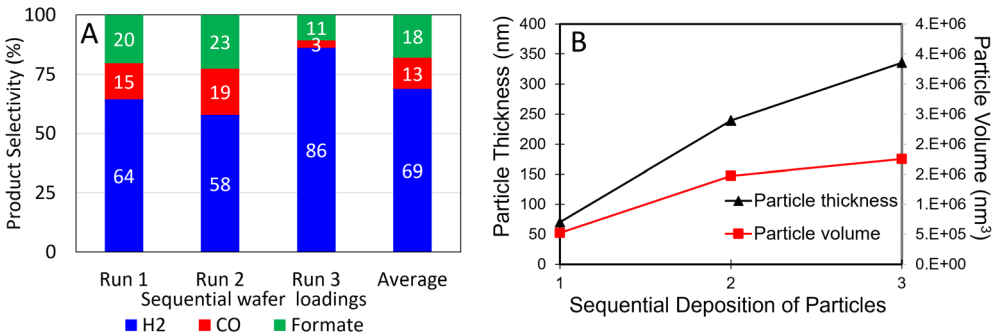

Fig. 6 Plots of the (A) product selectivities for **3**-PTI/HCuCl particles when deposited sequentially from a solution at −1.4 V *vs.* Ag/AgCl, and (B) the range of particle sizes deposited onto the surface when re-suspended into solution *via* sonication and measured by DLS.

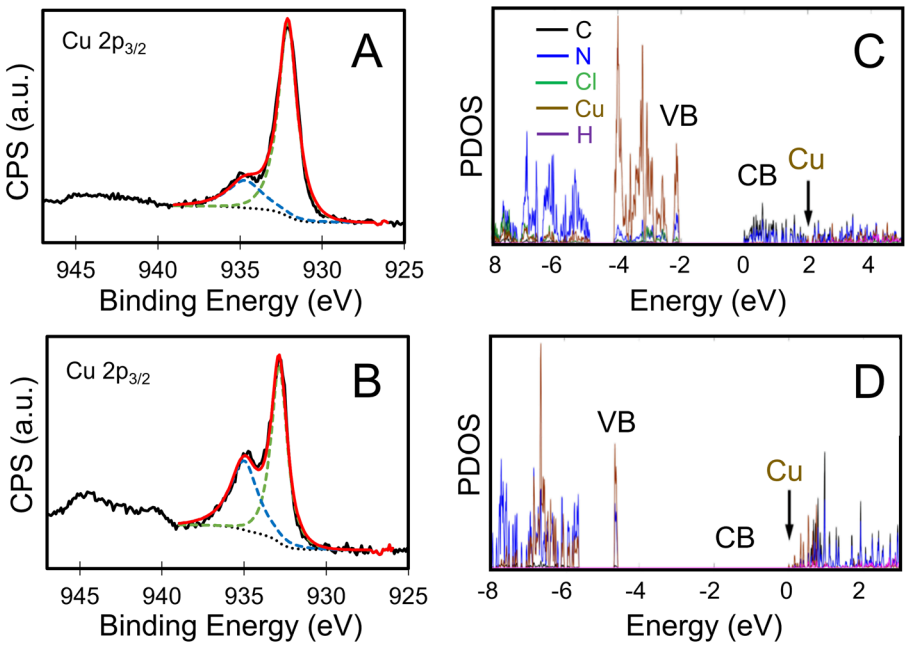

Fig. 7 *Ex situ* XPS high resolution spectra Cu $2p_{3/2}$ region for **3**-PTI/HCuCl before reaction (A) and after reaction on the electrode (B), including experimental (black-solid), background (black-dotted), fitted Cu(0)/Cu(I) peak (green-dashed), fitted Cu(II) peak (blue-dashed), and total fitted signal (red-solid). Results of calculated projected density of states (PDOS) on atomic orbitals, based on the quasi-particle energies obtained at G_0W_0@PBE0 level of theory for (C) bulk PTI/Cu and (D) monolayer PTI/Cu. Conduction band minimum (CBM) is set as the reference energy (*i.e.*, E = 0 eV).

Cu cations impacts the electronic structure of PTI and the ability to facilitate CO_2R at its band edges.[26] Specifically, the GW method was utilized in the framework of many-body Green's function theory, starting with PBE0 hybrid exchange–correlation density functional theory (DFT) calculation.[30–32] Fig. 7(C and D) shows the atom-projected density of states (DOS) of the bulk and monolayer form of PTI/Cu. The main difference in the DOS is observed in the band gap and conduction band (CB) energy. As the bulk PTI becomes more of two-dimensional (2D) and reaches a monolayer limit, the band gap increases as expected due to the quantum confinement effect. Interestingly, Cu-based states increasingly shift to dominate at the bottom of the CB edge. We note that this energy lowering of the metal cation states is not unique to the Cu(I) cation but also found for the Li case, *i.e.*, PTI/LiCl (see ESI†). While the PTI/Cu crystallites have different sizes and thicknesses, these results indicate that the highest activities for CO_2R are associated with the concomitant shifting of the Cu states closer to the CB edge with decreasing particle thickness. The maximal rates should thus be obtainable close to the monolayer limits, consistent with the CO_2R experiments, *i.e.*, runs 1 and 2 in Fig. 6A with the smallest particles.

Density-functional theory calculations were employed to elucidate the thermodynamics of the electrocatalytic reduction of CO_2 to CO and formate. With the benefit of a defined crystalline structure allowing more accurate computational modeling of mechanistic reaction pathways to CO_2R products, one aim was to shed light on the large difference in CO_2R observed between one Cu and two Cu atoms per cavity. Shown in Fig. 8 is the resulting mechanistic scheme for a PTI/Cu_2 cavity with the calculated binding energies and reduction potentials. The first and second reduction potentials of the starting complex were calculated. However, due to the instability of the doubly reduced complex, only the calculated first reduction potential of −1.1 V *vs.* SHE is shown. To begin the catalytic cycle, adsorption of CO_2 by the two Cu sites of the complex ($[PTI\text{-}Cu_2]^+$) may occur either before or after the one-electron reduction. The free energy of CO_2 binding after the first reduction (−2.82 kcal mol^{-1}) is more favorable than the initial binding of CO_2 to the two Cu sites of the starting complex (+4.03 kcal mol^{-1}). This occurs because of shifting of the two Cu atoms closer together after reduction. The reduction potential after CO_2 binding (**2b** to **3**) is −1.04 V *vs.* SHE. Based on the reasonable agreement between the first reduction potential at the applied bias potential of about −0.75 V *vs.* SHE in Fig. 2, as well as the calculated exergonic CO_2 binding energy after the first reduction, this indicates that CO_2 binds to the two Cu atoms after their reduction which begins the catalytic cycle. The coordinated CO_2 complex (**3**; [PTI-Cu_2-CO_2]) can undergo a reduction reaction followed by protonation or protonation followed by reduction to form the intermediate, [**5**; PTI-Cu-COOH]. Next, subsequent protonation of the intermediate on the terminal hydroxyl group and the release of H_2O steers the cycle towards CO formation, while protonation of the carbon leads to formate. For the CO cycle, protonation with the release of H_2O is thermodynamically favorable, with a free energy change of −5.47 kcal mol^{-1}. Desorption of CO is an uphill process (ΔG = +14.89 kcal mol^{-1}), indicating that its

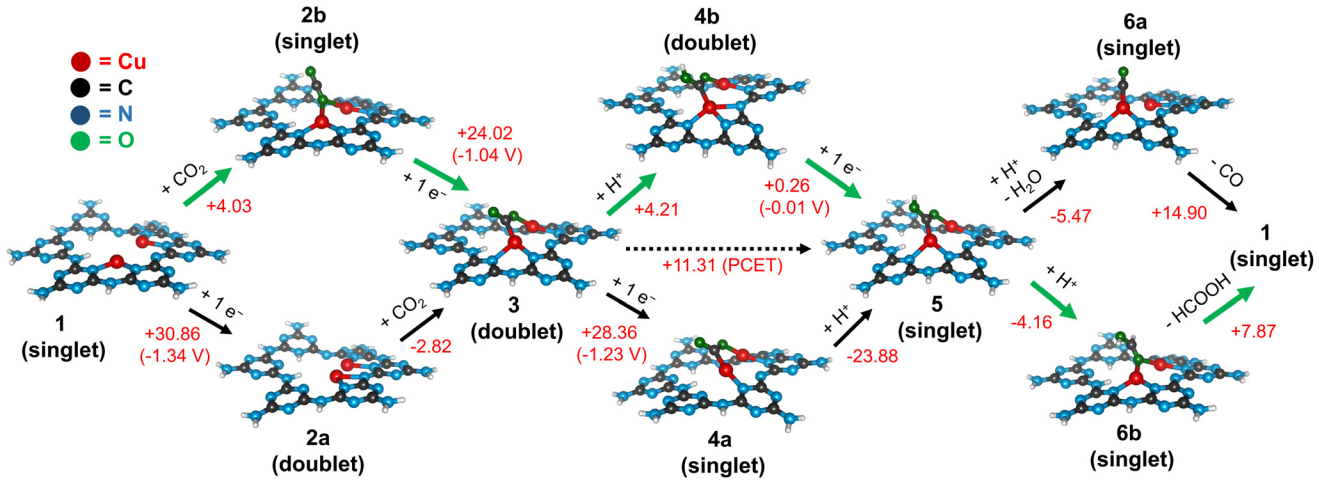

Fig. 8 Calculated catalytic mechanism of CO_2 reduction to either CO or HCOOH within an intralayer cavity of PTI containing two coordinated-Cu sites, with green arrows labeling the lowest energy pathway. Thermodynamic data reported in kcal mol^{-1} and redox potential in V *vs.* SHE (in parentheses).

release is less favorable. An uphill process is also observed for the desorption of formic acid (ΔG = +7.87 kcal mol^{-1}), at a relatively smaller free energy. The two-fold decrease in the free energy with the release of formate suggests its greater selectivity as compared to CO, as observed experimentally. Future studies could be aimed at preferential protonation of the terminal hydroxy group or carbon in intermediate **5** to achieve a higher product selectivity.

Calculations were also performed for PTI-Cu, *i.e.*, having only a single Cu atom coordinated within a cavity. The mechanistic pathway reveals a similar reaction mechanism of CO_2 reduction due to the same active site configuration, Cu–CO_2. However, a major difference was the much larger negative reduction potential for PTI-Cu, which suggested a larger amount of energy is needed to drive its CO_2 activation. A comparison of the relative sizes of the energetic steps for one Cu (PTI-Cu) *versus* two Cu (PTI-Cu_2) per cavity are shown plotted together in Fig. S18, ESI.† From the natural orbitals (NO) analysis of the reduced species (**2a**), Fig. S15,† electron reduction occurs on the ligand for PTI-Cu and on the metal (Cu–Cu) for PTI-Cu_2, thus resulting in a decreased Cu–Cu bond distance for PTI-Cu_2. These results suggest the cooperativity effect of the second Cu atom arises from the decreased Cu–Cu distance that results in a lowering of the reduction potential of PTI-Cu_2. This is in close agreement with experiment, with the greater FE of PTI/Cu_2Cl exhibited for CO_2R with its two Cu atoms per cavity. Also of note is the shifting of the Cu cation out of the plane of the intralayer cavity, especially after the second electron reduction. This would be expected from the change in local coordination environment preferences for Cu(0) *versus* Cu(I), where the former would be expected to shift out of the plane with its coordination being significantly weakened by increased antibonding interactions to the *N*-triazine groups. In molecular complexes, this feature highlights its tendency to decompose at the electrode surfaces with the loss of the free ligands and nucleation as metallic copper clusters. However, the rigid covalent framework of PTI/Cu maintains the ability of the Cu cations to re-coordinate at the end of the cycle.

Lastly, the product selectivity and overpotentials are competitive to those found in Cu-coordination complexes,[14] but with the current Cu-coordinated-PTI materials yielding significantly higher cathodic currents than in known molecular complexes. Also, these results compare to prior studies on electrocatalysis mediated by metallic-Cu(s) and Cu-coordinated carbon nitride materials, where the products of CO_2R typically yield a significantly different mixture of methane, carbon monoxide and ethanol.[45] For example, a recent, related study on the electrocatalytic CO_2 reduction by Cu-coordinated (~1.5 at%) PTI and PHI materials gave a high selectivity (>60%) for CH_4 within a gas diffusion electrode configuration.[46] Analogously, photoelectrochemical and photocatalytic CO_2 reduction studies on carbon nitride materials coordinated by Cu-catalyst sites at their surfaces have exhibited a high selectivity for either CH_4 or CO.[16,47] Thus, these comparatively lower Cu-loadings yield a different product selectivity. Conversely, the results of the current study demonstrate that a near-maximal coordination of Cu within both the bulk and surfaces of the PTI structure yields a higher selectivity for formate as the CO_2R product, consistent with the results of the mechanistic calculations.

IV. Conclusions

In summary, the coordination of copper within the intralayer cavities of crystalline poly(triazine imide) can be achieved using low temperature flux-based reactions with a CuCl, CuCl/KCl or KCl/$CuCl_2$ mixture at temperatures from 280 to 450 °C. The crystalline structures reveal that up to two Cu cations can be coordinated per intralayer cavity, depending on the reaction conditions. The micron-sized crystallites could be electrophoretically deposited onto glassy carbon and FTO substrates at

remarkably low applied biases of ~1.4 V, thus maintaining the particle integrity and crystalline structure without decomposition. This deposition process yields polycrystalline films with stable cathodic current densities ranging from ~5 to 50 mA cm^{-2} for the reduction of water and CO_2, the latter being favored for **2**-PTI/Cu_2Cl with the higher amount of intralayer copper sites and for thinner crystallites. Key discovered factors include the impact of multiple Cu coordination sites on the intermediate energies and CO_2R products. The results of calculations demonstrate a shift of the Cu-based states to the edge of the conduction band for thinner, exfoliated layers, and an energetic preference to produce formate over CO for two Cu-sites per intralayer cavity. Thus, the more ordered carbon-nitride structure helps to reveal new mechanistic insights into the CO_2R pathways relevant to Cu-containing materials and a deeper molecular-level understanding needed to optimize CO_2R in future investigations. In summary, a promising new approach has been demonstrated to coordinate Cu as well as other transition-metal cations within the intralayer cavities of crystalline carbon nitride to leverage its stable covalent framework for electrocatalytic reactions.

Author contributions

The manuscript was written through contributions of all authors. All authors have given approval to the final version of the manuscript.

Conflicts of interest

There are no conflicts to declare.

Acknowledgements

This material is based upon work solely supported as part of the Center for Hybrid Approaches in Solar Energy to Liquid Fuels (CHASE), an Energy Innovation Hub funded by the U.S. Department of Energy, Office of Science, Office of Basic Energy Sciences under Award Number DE-SC0021173. SEM was carried out at the Analytical Instrumentation Facility (AIF) at North Carolina State University, and XPS was conducted at Duke University Shared Materials Instrumentation Facility (SMIF), supported by the state of North Carolina and the National Science Foundation (Award Number ECCS-2025064). The AIF and SMIF are members of the North Carolina Research Triangle Nanotechnology Network (RTNN), a site in the National Nanotechnology Coordinated Infrastructure (NNCI).

References

1 W. Ju, A. Bagger, G. Hao, A. So, I. Sinev, V. Bon, B. R. Cuenya, S. Kaskel, J. Rossmeisl and P. Strasser, Understanding Activity and Selectivity of Metal-Nitrogen-Doped Carbon Catalysts for Electrochemical Reduction of CO2, *Nat. Commun.*, 2017, **8**(944), 1–9.

2 A. So, W. Ju, A. Bagger, P. Franco, J. Rossmeisl and P. Strasser, Electrochemical Reduction of CO_2 on Metal-Nitrogen-Doped Carbon Catalysts, *ACS Catal.*, 2019, **9**, 7270–7284.

3 C. Cometto, A. Ugolotti, E. Grazietti, A. Moretto, G. Bottaro, C. D. Valentin, L. Calvillo and G. Granozzi, Copper Single-Atoms Embedded in 2D Graphitic Carbon Nitride for the CO_2 Reduction, *npj 2D Mater. Appl.*, 2021, 1–11.

4 C. Ding, C. Feng, Y. Mei, F. Liu, H. Wang, M. Dupuis and C. Li, Applied Catalysis B: Environmental Carbon Nitride Embedded with Transition Metals for Selective Electrocatalytic CO_2 Reduction, *Appl. Catal., B*, 2020, **268**, 118391.

5 H. Yu, H. Cohen and R. Neumann, Photoelectrochemical Reduction of Carbon Dioxide with a Copper Graphitic Carbon Nitride Photocathode, *Chem. – Eur. J.*, 2021, (27), 13513–13517.

6 S. Paul, Y. Kao, L. Ni, R. Ehnert, I. Herrmann-geppert, R. Van De Krol, R. W. Stark, W. Jaegermann, U. I. Kramm and P. Bogdano, Influence of the Metal Center in M–N–C Catalysts on the CO_2 Reduction Reaction on Gas Diffusion Electrodes, *ACS Catal.*, 2021, (11), 5850–5864.

7 V. W. Lau and B. V. Lotsch, A Tour-Guide through Carbon Nitride-Land: Structure- and Dimensionality-Dependent Properties for Photo (Electro) Chemical Energy Conversion and Storage, *Adv. Energy Mater.*, 2022, **12**, 1–26.

8 E. Wirnhier, M. Döblinger, D. Gunzelmann, J. Senker, B. V. Lotsch and W. Schnick, Poly(Triazine Imide) with Intercalation of Lithium and Chloride Ions $[(C_3N_3)_2(NH_xLi_{1-x})_3.LiCl]$: A Crystalline 2D Carbon Nitride Network, *Chem. – Eur. J.*, 2011, **17**(11), 3213–3221.

9 M. B. Mesch, K. Bärwinkel, Y. Krysiak, C. Martineau, F. Taulelle, R. B. Neder, U. Kolb and J. Senker, Solving the Hydrogen and Lithium Substructure of Poly(Triazine Imide)/LiCl Using NMR Crystallography, *Chem. – Eur. J.*, 2016, **22**(47), 16878–16890.

10 M. Pauly, J. Kröger, V. Duppel, C. Murphey, J. Cahoon, B. V. Lotsch and P. A. Maggard, Unveiling the Complex Configurational Landscape of the Intralayer Cavities in a Crystalline Carbon, *Chem. Sci.*, 2022, **13**, 3187–3193.

11 J. Wang, D. Hao, J. Ye and N. Umezawa, Determination of Crystal Structure of Graphitic Carbon Nitride: Ab Initio Evolutionary Search and Experimental Validation, *Chem. Mater.*, 2017, **29**(7), 2694–2707.

12 T. M. Suter, T. S. Miller, J. K. Cockcroft, A. E. Aliev, M. C. Wilding, A. Sella, F. Corà, C. A. Howard and P. F. McMillan, Formation of an Ion-Free Crystalline Carbon Nitride and Its Reversible Intercalation with Ionic Species and Molecular Water, *Chem. Sci.*, 2019, **10**(8), 2519–2528.

13 S. Roy, Z. Li, Z. Chen, A. C. Mata, P. Kumar, S. Ch, I. F. Teixeira, I. F. Silva, G. Gao, N. V. Tarakina, G. Kibria, C. V. Singh, J. Wu and P. M. Ajayan, Cooperative Copper

Single Atom Catalyst in Two-Dimensional Carbon Nitride for Enhanced CO_2 Electrolysis to Methane, *Adv. Mater.*, 2023, **2300713**, 1–32.

14 K. Kim, P. Wagner, K. Wagner and A. J. Mozer, Electrochemical CO_2 Reduction Catalyzed by Copper Molecular Complexes: The Influence of Ligand Structure, *Energy Fuels*, 2022, **36**, 4653–4676.

15 Z. Weng, Y. Wu, M. Wang, J. Jiang, K. Yang, S. Huo, X. Wang, Q. Ma, G. W. Brudvig, V. S. Batista, Y. Liang, Z. Feng and H. Wang, Active Sites of Copper-Complex Catalytic Materials for Electrochemical Carbon Dioxide Reduction, *Nat. Commun.*, 2018, 1–9.

16 Z. Li, B. Li, D. Zhang, L. Cheng and Q. Zhang, Crystalline Carbon Nitride Supported Copper Single Atoms for Photocatalytic CO_2 Reduction with Nearly 100% CO Selectivity, *ACS Nano*, 2020, **14**, 10552–10561.

17 L. Cheng, P. Zhang, Q. Wen, J. Fan and Q. Xiang, Copper and Platinum Dual-Single-Atoms Supported on Crystalline Graphitic Carbon Nitride for Enhanced Photocatalytic CO_2 Reduction, *Chin. J. Catal.*, 2022, **43**, 451–460.

18 L. Cheng, X. Yue, L. Wang, D. Zhang, P. Zhang, J. Fan and Q. Xiang, Dual-Single-Atom Tailoring with Bifunctional Integration for High-Performance CO_2 Photoreduction, *Adv. Mater.*, 2021, **33**, 2105135.

19 J. Jones, G. K. S. Prakash and G. A. Olah, Electrochemical CO_2 Reduction : Recent Advances and Current Trends, *Isreal J. Chem.*, 2014, **1661**, 1451–1466.

20 Y. Pei, A Brief Review of Electrocatalytic Reduction of CO_2 Materials, Reaction Conditions, and Devices, *Energy Sci. Eng.*, 2021, **9**, 1012–1032.

21 M. R. Dubois and D. L. Dubois, Development of Molecular Electrocatalysts for CO_2 Reduction and H_2 Production/Oxidation, *Acc. Chem. Res.*, 2009, **42**(12), 1974–1982.

22 S. Mcguigan, S. J. Tereniak, C. L. Donley, A. Smith, S. Jeon, F. Zhao, R. N. Sampaio, M. Pauly, L. Keller, L. Collins, G. N. Parsons, T. Lian, E. A. Stach and P. A. Maggard, Discovery of a Hybrid System for Photocatalytic CO_2 Reduction via Attachment of a Molecular Cobalt-Quaterpyridine Complex to a Crystalline Carbon Nitride, *ACS Appl. Energy Mater.*, 2023, (6), 10542–10553.

23 N. Sonoyama, M. Kirii and T. Sakata, Electrochemical Reduction of CO_2 at Metal-Porphyrin Supported Gas Diffusion Electrodes under High Pressure CO_2, *Electrochem. Commun.*, 1999, **1**, 213–216.

24 NIST Standard Reference Database 31 **https://www.nist.gov/srd/nist-standard-reference-database-31** (accessed Jun 12, 2023).

25 M. S. Hybertsen and S. G. Louie, First-Principles Theory of Quasiparticles: Calculation of Band Gaps in Semiconductors and Insulators, *Phys. Rev. Lett.*, 1985, **55**(13), 1418–1421.

26 G. Onida, I. Nazionale, R. T. Vergata, R. Scientifica and I. Roma, Electronic Excitations : Density-Functional versus Many-Body Green's-Function Approaches, *Rev. Mod. Phys.*, 2002, **74**, 601–659.

27 P. Giannozzi, S. Baroni, N. Bonini, M. Calandra, R. Car, C. Cavazzoni, D. Ceresoli, G. L. Chiarotti, M. Cococcioni, I. Dabo, A. D. Corso, S. D. Gironcoli, S. Fabris, G. Fratesi, R. Gebauer, U. Gerstmann, C. Gougoussis, A. Kokalj, M. Lazzeri, L. Martin-samos, N. Marzari, F. Mauri, R. Mazzarello, S. Paolini, A. Pasquarello, L. Paulatto, C. Sbraccia, A. Smogunov and P. Umari, QUANTUM ESPRESSO: A Modular and Open-Source Software Project for Quantum Simulations of Materials, *J. Phys.: Condens. Matter*, 2009, **21**, 1–19.

28 M. Schlipf and F. Gygi, Optimization Algorithm for the Generation of ONCV Pseudopotentials, *Comput. Phys. Commun.*, 2015, **196**, 36–44.

29 D. R. Hamann, Optimized Norm-Conserving Vanderbilt Pseudopotentials, *Phys. Rev. B: Condens. Matter Mater. Phys.*, 2013, **88**(8), 85117–85127.

30 J. P. Perdew, M. Ernzerhof and K. Burke, Rationale for Mixing Exact Exchange with Density Functional Approximations, *J. Chem. Phys.*, 1996, **105**, 9982–9985.

31 I. Carnimeo, S. Baroni and P. Giannozzi, Fast Hybrid Density-Functional Computations Using Plane-Wave Basis Sets Fast Hybrid Density-Functional Computations Using Plane-Wave Basis Sets, *Electron. Struct.*, 2019, **1**, 15009.

32 J. Deslippe, G. Samsonidze, D. A. Strubbe, M. Jain, M. L. Cohen and S. G. Louie, BerkeleyGW: A Massively Parallel Computer Package for the Calculation of the Quasiparticle and Optical Properties of Materials and Nanostructures, *Comput. Phys. Commun.*, 2012, **183**(6), 1269–1289.

33 H. J. Monkhorst and J. D. Pack, Special Points for Brillonin-Zone Integrations, *Phys. Rev. B: Solid State*, 1976, **13**(12), 5188–5192.

34 A. D. Becke, Density-Fnnctional Exchange-Energy Approximation with Correct Asymptotic Behavior, *Phys. Rev. A*, 1988, **4**(4), 276–282.

35 R. Krishnan, J. S. Binkley, R. Seeger and J. A. Pople, Self–Consistent Molecular Orbital Methods. XX. A Basis Set for Correlated Wave Functions, *J. Chem. Phys.*, 1979, **72**, 650–654.

36 A. D. Mclean and G. S. Chandler, Contracted Gaussian Basis Sets for Molecular Calculations. I. Second Row Atoms, Z=11-18, *J. Chem. Phys.*, 1980, **72**, 5639–5648.

37 M. Dolg, U. Wedig, H. Stoll and H. Preuss, Energy–adjusted Ab Initio Pseudopotentials for the First Row Transition Elements, *J. Chem. Phys.*, 1987, **86**, 866–872.

38 G. Scalmani and M. J. Frisch, Continuous Surface Charge Polarizable Continuum Models of Solvation. I. General Formalism, *J. Chem. Phys.*, 2010, **132**, 1–15.

39 L. E. Roy, E. Jakubikova, M. G. Guthrie and E. R. Batista, Calculation of One-Electron Redox Potentials Revisited. Is It Possible to Calculate Accurate Potentials with Density Functional Methods?, *J. Phys. Chem. A*, 2009, **113**, 6745–6750.

40 M. J. Frisch, G. W. Trucks, H. B. Schlegel, G. E. Scuseria, M. A. Robb, J. R. Cheeseman, G. Scalmani, V. Barone, G. A. Petersson, H. Nakatsuji, X. Li, M. Caricato, A. V. Marenich, J. Bloino, B. G. Janesko, R. Gomperts,

B. Mennucci, H. P. Hratchian, J. V. Ortiz, and D. J. Fox, *Gaussian 16. Revision C.01*, Gaussian, Inc., Wallingford CT, 2016.

41 C. Z. Liao, V. W. H. Lau, M. Su, S. Ma, C. Liu, C. K. Chang, H. S. Sheu, J. Zhang and K. Shih, Unraveling the Structure of the Poly(Triazine Imide)/LiCl Photocatalyst: Cooperation of Facile Syntheses and a Low-Temperature Synchrotron Approach, *Inorg. Chem.*, 2019, **58**(23), 15880–15888.

42 L. Besra and M. Liu, A Review on Fundamentals and Applications of Electrophoretic Deposition (EPD), *Prog. Mater. Sci.*, 2007, **52**, 1–61.

43 J. Xu and M. Shalom, Electrophoretic Deposition of Carbon Nitride Layers for Photoelectrochemical Applications, *ACS Appl. Mater. Interfaces*, 2016, **8**, 13058–13063.

44 M. C. Biesinger, Advanced Analysis of Copper X-Ray Photoelectron Spectra, *Surf. Interface Anal.*, 2017, **49**, 1325–1334.

45 S. Nitopi, E. Bertheussen, S. B. Scott, X. Liu, A. K. Engstfeld, S. Horch, B. Seger, I. E. L. Stephens, K. Chan, C. Hahn, J. K. Nørskov, T. F. Jaramillo and I. Chorkendor, Progress and Perspectives of Electrochemical CO_2 Reduction on Copper in Aqueous Electrolyte, *Chem. Rev.*, 2019, **119**, 7640–7672.

46 S. Roy, Z. Li, Z. Chen, A. C. Mata, P. Kumar, S. C. Sarma, I. F. Teixeira, I. F. Silva, G. Gao, N. V. Tarakina, M. G. Kibria, C. V. Singh, J. Wu and P. M. Ajayan, Cooperative Copper Single-Atom Catalyst in 2D Carbon Nitride for Enhanced CO_2 Electrolysis to Methane, *Adv. Mater.*, 2023, 2300713.

47 G. Huang, Q. Niu, Y. He, J. Tian, M. Gao, C. Li, N. An, J. Bi and J. Zhang, Spatial Confinement of Copper Single Atoms into Covalent Triazine-Based Frameworks for Highly Efficient and Selective Photocatalytic CO_2 Reduction, *Nano Res.*, 2022, **15**, 8001–8009.

